Journal of Molecular Neuroscience (2022) 72:527–543
https://doi.org/10.1007/s12031-021-01896-6

# Age-related LRRK2 G2019S Mutation Impacts Microglial Dopaminergic Fiber Refinement and Synaptic Pruning Involved in Abnormal Behaviors

Qiuyang Zhang[1,2,3,4] · Xiaojuan Cheng[1,2,3,4] · Wei Wu[6] · Siyu Yang[1,2,3] · Hanlin You[1,2,3,4] · Zucheng Ye[6] · Nan Liu[1,3,4,5] · Xiaochun Chen[1,3,4] · Xiaodong Pan[1,2,3,4,6]

Received: 24 May 2021 / Accepted: 24 July 2021 / Published online: 19 August 2021


## Abstract

Mutations in the leucine-rich repeat kinase 2 (LRRK2) gene are the most frequent cause of autosomal dominant Parkinson's disease (PD), producing psychiatric and motor symptoms. We conducted this study to explore whether microglial dopaminergic (DAergic) fiber refinement and synaptic pruning are involved in the abnormal behavioral phenotypes of carriers of the LRRK2 G2019S mutation, by employing young and middle-aged PD model mice. The results revealed a characteristic late-onset hyperactivity and a progressive decline in the motor coordination of the LRRK2 G2019S mutation mice. LRRK2 G2019S mutation-induced aberrant microglial morphogenesis, with more branches and junctions per cell, resulted in excessive microglial refinement of dopaminergic (DAergic) fibers. Moreover, aberrant synaptic pruning distinctly impacted the prefrontal cortex (PFC) and dorsal striatum (DS), with significantly higher spine density in the PFC but the opposite effects in the DS region. Furthermore, LRRK2 G2019S mutation remodeled the inflammatory transcription landscape of microglia, rendering certain cerebral areas highly susceptible to microglial immune response. These findings indicate that LRRK2 G2019S mutation induces the production of inflammatory cytokines and mediates abnormal microglial morphogenesis and activity, resulting in abnormal phagocytosis, synaptic pruning and loss of DAergic fibers during aging, and, eventually, PD-related behavioral abnormalities.

**Keywords** LRRK2 G2019S mutation · Microglia · DAergic fiber refinement · Synaptic pruning · Abnormal behaviors

Qiuyang Zhang, Xiaojuan Cheng These authors contributed equally to this work.

✉ Xiaodong Pan
pxd77316@163.com

1 Department of Neurology, Fujian Medical University Union Hospital, 29 Xinquan Road, Fuzhou 350001, China

2 Fujian Institute of Geriatrics, Fujian Medical University Union Hospital, 29 Xinquan Road, Fuzhou 350001, China

3 Institute of Clinical Neurology, Fujian Medical University, 29 Xinquan Road, Fuzhou 350001, China

4 Fujian Key Laboratory of Molecular Neurology, Fujian Medical University, 88 Jiaotong Road, Fuzhou 350001, China

5 Department of Rehabilitation, Fujian Medical University Union Hospital, 29 Xinquan Road, Fuzhou 350001, China

6 Key Laboratory of Brain Aging and Neurodegenerative Diseases, Fujian Medical University, 1 Xueyuan Road, Fuzhou 350001, China

**Abbreviations**

| | |
|---|---|
| PD | Parkinson's disease |
| LRRK2 | Leucine-rich repeat kinase 2 |
| DA | Dopaminergic |
| DAT | Dopamine transporter |
| TH | Tyrosine hydroxylase |
| CD68 | Cluster of differentiation 68 |
| DS | Dorsal striatum |
| GS | LRRK2 G2019S mutation mice |
| Iba1 | Ionized calcium binding adaptor molecule 1 |
| PFC | Prefrontal cortex |
| PSD95 | Postsynaptic density protein 95 |
| VGLUT1 | Vesicular glutamate transporter 1 |

## Introduction

Parkinson's disease (PD), a slowly progressive neurodegenerative disorder, impairs motor function, causing a spectrum of neuropsychiatric symptoms. Corroborative evidence from several lines of research suggests that leucine-rich repeat

kinase 2 (LRRK2) G2019S mutation plays a critical role in late-onset PD (Mancini et al. 2020; Sheerin et al. 2014). While aging is regarded as a primary risk factor for PD pathogenesis, the penetrance of LRRK2 G2019S (Xiao et al. 2015) in PD increases robustly with aging as well: from 28% at the age of 59 to 51% at the age of 69 (Healy et al. 2008). Mice with the LRRK2 G2019S mutation also show a loss of striatal dopaminergic (DAergic) terminals, with aging as a major determinant of the effect (Chou et al. 2014; Novello et al. 2018; Xu et al. 2012). LRRK2 is particularly enriched in the striatum and prefrontal cortex (PFC), but quite limited in the midbrain (Giesert et al. 2013; Mandemakers et al. 2012). This disparate expression pattern implies that LRRK2 may play a distinct role in responding to the regional stimulation from dopamine (DA) and other neurotransmitters in the striatum and PFC, which are associated with motor dysfunction and neuropsychiatric abnormalities. However, it remains to be elucidated how LRRK2 G2019S mutation is implicated in the loss of striatal DAergic fibers and neuropathological change of PFC in PD-associated abnormal motor and neuropsychiatric behaviors during aging.

Microglia play an important role in the monitoring of synaptic function and the repair of neural circuits (Ikegami et al. 2019). Microglial activation and abnormal synaptic pruning have been reported in several psychomotor disorders, including PD and schizophrenia (Matikainen-Ankney et al. 2018; Sellgren et al. 2019). Activated microglia can secrete a variety of inflammatory mediators, including cytokines and chemokine, which promote the damage to the neurons and synapses in PD (Ho 2019). LRRK2 is richly expressed in the microglia of the primary phagocytes of the mammalian brain (Gardet et al. 2010; Hakimi et al. 2011). Recent reports indicate that LRRK2 G2019S mutation impacts microglial activity, resulting in disordered microglial phagocytosis and migration. Moreover, the activity of microglia also changes with aging (Harry 2013). However, it remains unclear how LRRK2 G2019S mutation impacts aging-related abnormal microglial synaptic pruning in specific brain regions of PD.

Notably, the injured DAergic fibers and synaptic components may be sensitive indicators of the advance of the PD course. Meanwhile, age-related deficits in brain function may occur due to the reconstruction of microglia-related neural circuits, which is closely related with abnormal behaviors (Lee et al. 2019). To date, little literature is available regarding the impacts and potential contribution of abnormal microglial activity on DAergic fibers and synapses in LRRK2 G2019S mutant mice.

Here, we explored whether microglial DAergic fiber refinement and synaptic pruning are involved in the abnormal behavioral phenotypes of carriers of LRRK2 G2019S mutations by employing young and middle-aged PD model mice. We revealed a new pathogenic mechanism of the LRRK2 G2019S mutation, in which it alters the microglial function in the neurodegeneration in PD brains during aging. This knowledge may facilitate the identification of the features of microglial function in the prodromal and late stages of PD, and pave the way for effective clinical interventions of microglial modulation as a candidate target.

## Materials and Methods

### Mice

BAC LRRK2 (G2019S) mice (Stock 018,785) were purchased from Jackson Laboratories. Male wild-type (WT) and transgenic littermate mice were obtained by breeding heterozygotes. As gender may affect the biological behavior or pathophysiological changes of mice in the process of aging (Kundey et al. 2019), we only selected male mice for research in order to minimize the impact of gender differences, including the effect of estrogen on cognition and other behaviors. The genotypes were confirmed by polymerase chain reaction (PCR) analysis of tail biopsy specimens. The environment was maintained at a steady ambient temperature on a 12/12-h light/dark cycle, and the mice had access to food and water ad libitum. All behavioral tests were conducted during the light phase of the cycle, specifically between 9 am and 5 pm.

### Open-Field Test

As described previously (Nolan et al. 2017), the activity and anxiety levels of mice were measured with the Flex-Field activity system (SANS SA215, Saiangsi, Inc., China). Open-field software was used to trace and quantify the movement of the mice in the apparatus for 5 min.

### Rotarod Test

As described previously (Zhang et al. 2019), mice were placed onto a rotating rod that automatically accelerated from 0 to 40 rpm over 5 min (SANS SA102, Saiangsi, Inc., China). The length of time each mouse stayed on the rotating rod was recorded. The test was performed in triplicate.

### Gait Analysis

As described previously (Fernagut et al. 2002), each mouse was allowed to trot on a strip of paper (4.5 cm wide, 110 cm long) down a brightly lit runway towards a dark goal box. Each mouse was trained for 15 s at a speed of 8 cm/s. After 1 min of rest, the movements of the mouse were recorded. The stride length, sway length, and stance length were analyzed with ImageJ software.

## Cylinder Experiment

As described previously (Ip et al. 2017), mice were placed into a transparent Plexiglas cylinder (12 cm in diameter and 30 cm in height) and observed for 3 min. Each time the mice reared on their hind limbs, records were made to note how many times they touched the inner surface of the cylinder with the right forepaw, the left forepaw, or both simultaneously. The final index was calculated as percentage of right forepaw use according to the following equation: (right paw only + 0.5 both paws)/ (right paw only + left paw only + both paws) × 100%. With this index, we defined the forepaw usage preference as follows: 50%, representing symmetric use of both forepaws; < 50%, indicating a preference for the left forepaw; > 50%, signifying a preference for the right forepaw.

## Fear Conditioning

As described previously (Nolan et al. 2017), fear conditioning experiments were conducted in Quick Change test chambers (SANS SA218, Saiangsi, Inc., China). On the first day of testing, animals were transported to a holding room and allowed to acclimate for 30 min. They were then taken to a separate testing room and placed in fear conditioning chambers. The animals received two pairings of a 30-s, 80-dB white noise stimulus (the conditioned stimulus, or CS) and a 2-s, 0.7 mA shock stimulus (the unconditioned stimulus, or US) that immediately followed the white noise. After a 120-s interval, the second pairing of CS and US was proceeded. The trial lasted for a total of 760 s. Animals were then returned to the holding room, and the apparatus was cleaned with a 75% ethanol solution and dried thoroughly. The second day of testing consisted of two trials. In the first trial, the mice were placed in the familiar context and allowed to move freely for 300 s to evaluate freezing behavior in the original context. After 1 h, the animals underwent a second trial, in which the context was altered by changing the shape and floor of the chamber as well as adding a novel lemon odor emanating from under the floor grid. The animals were placed in the new context for 360 s. For the first 150 s, they were allowed to acclimate to the novel context; then, they were presented with the CS continuously for 30 s and allowed to move freely for another 3 min. The freezing behavior of the mice was examined.

## RT–qPCR Analysis

RNA extraction, cDNA production, and SYBR Green-based qPCR were performed as described previously (Bonnard et al. 2020). The primer sequences used are summarized in Table 1. The mRNA expression was normalized to glyceraldehyde 3-phosphate dehydrogenase (GAPDH) as indicated. The analysis programs were written in R programming language (v. 3.6.3), and the relationships between variables were visualized as a heat map with the "pheatmap" R package (v. 1.0.12).

## Golgi Staining

Golgi staining was performed using the manufacturer's protocols (Hito Golgi-Cox OptimStain™ Kit, USA). Spine density was measured based on the secondary branches of apical dendrites of pyramidal neurons located in the prefrontal cortex and medium spiny neurons from the dorsal striatum. A total of 20 neurons per animal ($N = 3$ mice) were evaluated.

## Brain Tissue Treatment (Immunohistochemistry and Immunofluorescence)

Mice were anesthetized with a ketamine (100 mg $kg^{-1}$)/xylazine (20 mg $kg^{-1}$) cocktail and perfused with 0.9% saline, followed by fixation with 4% paraformaldehyde (PFA) for 6 h and subsequent incubation of the brains in 30% sucrose for 48 h. For immunohistochemistry (IHC) staining, 40 µm sagittal slices were obtained with a Leica CM1950 freezing microtome. The IHC was measured according to a procedure published previously (Pan et al. 2019). The primary antibody was mouse monoclonal LRRK2 antibody (1:300, MABN40; Millipore, Darmstadt, Germany). Images were captured using an Olympus microscope (Olympus, Tokyo, 163–0914, Japan). LRRK2-positive particles were quantified using the "Analyze Particles" function of ImageJ software, which provides the average optical density. For immunofluorescence staining, the brains were sectioned into slices (40 µm coronal slices) on a Leica freezing microtome, permeabilized in Tris-buffered saline (TBS) with 0.3% Triton X-100, and finally blocked with 10% normal donkey serum. For immunofluorescence staining, the sections were incubated with antibodies against ionized calcium-binding adapter molecule 1 (Iba1, #019–19,741, 1:1000; Wako, Osaka, Japan), tyrosine hydroxylase (TH, sc-25269, 1:500; Santa Cruz Biotech, Dallas, Texas), dopamine transporter (DAT, MAB369, 1:500; Millipore, MA, USA), postsynaptic density protein 95 (PSD95, MAB1956, 1:500; Millipore), and vesicular glutamate transporter 1 (VGLUT1, 135,304, 1:1000; Synaptic System, Goettingen, Germany). Immunoreactive structures were detected with Alexa Fluor donkey anti-mouse, anti-rabbit, or anti-rat secondary antibodies in the 488-, 594-, or 647-nm range (1:2000; Invitrogen, Carlsbad, CA, USA). Nuclei were stained with DAPI (1:5000; Invitrogen). Fluorescence images were captured under a confocal laser scanning microscope (LSM 780; Zeiss, Thornwood, NJ, USA).

**Table 1** Sequence of Q-PCR primers

| Gene name | Forward primer (5' to 3') | Reverse primer (5' to 3') |
|---|---|---|
| GAPDH | CAGTGGCAAAGTGGAGATTGTTG | CTCGCTCCTGGAAGATGGTGAT |
| C1qa | GACTGAAGGGCGTGAAAGG | ATGGACTCTCCTGGTTGGTG |
| C3 | CTGGCCCTGATGAACAAACT | GGATGTGGCCTCTACGTTGT |
| C3aR | GTGCAAACTTATCCCATCCATC | GTACTATCAGACATCGGTCCAG |
| CR1 | GGATACAGAACAGTAAGTCGCT | CAGGTAGAAAGGTCTGAGGAAG |
| IL-1α | ATCAGCAACGTCAAGCAACG | GGTTGGATGGTCTCTTCCAGA |
| TNF-α | ACTGGCAGAAGAGGCACTCC | GCCACAAGCAGGAATGAGAA |
| iNOS | CCTCCTCGTTCAGCTCACCT | CAATCCACAACTCGCTCCAA |
| TGF-β | CCAGATCCTGTCCAAACTAAGG | CTCTTTAGCATAGTAGTCCGCT |
| Arg1 | CAATGAAGAGCTGGCTGGTG | GGCCAGAGATGCTTCCAACT |
| Ym1 | AAGGAGCCACTGAGGTCTGG | TTGTCCTTGAGCCACTGAGC |
| IL-6 | ACTTCCATCCAGTTGCCTTCTTGG | TTAAGCCTCCGACTTGTGAAGTGG |
| IFN-γ | CTTGAAAGACAATCAGGCCATC | CTTGGCAATACTCATGAATGCA |
| Trem2 | TCATGTACTTATGACGCCTTGA | GAGGTTCTTCAGAGTGATGGTG |
| Tmem119 | GGCTGACATTCTGGCTGCTACC | CTCCTCCGACCCACCCTTCAC |
| PU.1 | GGCTGACATTCTGGCTGCTACC | CTCCTCCGACCCACCCTTCAC |
| CX3CR1 | CATGTGCAAGCTCACGACTG | TCCGGTTGTTCATGGAGTTG |
| SORL1 | CCAAACGCTATCTACATTGAGC | GCAAACATATACTTGTCGCGAA |
| P2RY12 | CCTGCCTTGATCCATTCATCTA | GTCCTTTCTTCTTGTTTGTCCC |
| CD33 | ACTCCTGACATTATAATCCCGG | TTGACATCCAGGAGAAAGTAGG |
| CSF1R | CTCTTCACTCCGGTGGTGGT | GCACCTGGTACTTCGGCTTC |
| ABCA7 | AACCATGGAATTTCCCTTTTCG | TCGTAGAAGTCAAGGTTGAGTC |
| IL-4 | TACCAGGAGCCATATCCACGGATG | TGTGGTGTTCTTCGTTGCTGTGAG |

## Dendritic Spine Analysis

Images of the prefrontal cortex and the dorsal striatum (DS) were acquired using an LSM 780 × 100/1.4 oil objective (Zeiss). Each image consisted of a stack of images taken across the z-plane of the PFC and the DS neurons. Spine analysis was performed with ImageJ software (Fiji, ImageJ 1.46, NIH, Bethesda, MD, USA). Three independent replications were performed for each experimental setting.

## Image Analysis

The paired images in all the figures were collected at the same gain and offset settings and subjected to uniform

post-collection processing. The images were either presented as a single optic layer after acquisition in z-series stack scans from individual fields or displayed as maximum intensity projections to represent confocal stacks. For quantitative assessment of the accumulation of protein and the distributions of various markers, images were obtained using identical settings and exported to ImageJ software for image analyses. Images were converted to an 8-bit color scale (fluorescence intensity from 0 to 255). Areas of interest were first selected by the polygon or freehand selection tools and then subjected to measurement by area fractions. All images were acquired and quantified by a user blinded to the experimental design. For microglial counts and morphologic analysis, confocal images for the selected marker Iba1 were modified as 8-bit and Z-stack projection images. Iba1 and DAPI$^+$ cells were counted per high-power field (HPF). The resulting images were smoothed, binarized, and skeletonized using the Skeletonize Plugin in ImageJ (Arganda-Carreras et al. 2010). The resulting images were processed by choosing the Analyze Skeleton 2D 3D option in the Skeletonize Plugin, and the number of branches and junctions per cell were obtained from the Results tables. The junction index is commonly used to evaluate microglial morphology (Filipello et al. 2018). For the density of VGLUT1$^+$ and PSD95$^+$ analyses, a max intensity threshold, with a lower limit of 58 and 60, respectively, and an upper limit of 255, was applied using the "Analyze Particles" function in Fiji.

### Statistical Analysis

Statistical tests were performed using GraphPad Prism 6.0 (GraphPad Software, San Diego, CA, USA). Statistical significance was determined by comparing the means of different groups using the two-tailed Student's *t*-test and two-way ANOVA analysis. In all figures, error bars represent the mean ± SEM. A *p*-value of ≤ 0.05 was considered statistically significant.

## Results

### Different Behavioral Performance in LRRK2 G2019S Mutant Mice and WT Mice During Aging

To evaluate the impact of LRRK2 malfunction on age-dependent behavioral alterations, we conducted a battery of behavioral tests on 2- and 10-month-old WT and *Lrrk2*$^{-G2019S}$ mice. The current study found that, compared with age-matched WT mice, 2-month-old *Lrrk2*$^{-G2019S}$ mice spent a significantly reduced amount of time in the center of the open field ($p < 0.01$; Fig. 1a and c); compared with the age-matched WT mice, the 10-month-old *Lrrk2*$^{-G2019S}$ mice spent significantly more activity time in the center of the open field and the peripheral trajectory (WT: 4.90 ± 0.96%, *Lrrk2*$^{-G2019S}$: 16.61 ± 1.27%, $p < 0.0001$; WT: 9.82 ± 1.02 m, *Lrrk2*$^{-G2019S}$: 14.49 ± 0.99 m, $p < 0.05$; Fig. 1a and c), suggesting that the abnormal neuropsychological behavior of the *Lrrk2*$^{-G2019S}$ mice is greatly enhanced. Meanwhile, compared with the age-matched controls, the middle-aged *Lrrk2*$^{-G2019S}$ mice moved at a higher speed (WT: 36.56 ± 4.02 mm/s, *Lrrk2*$^{-G2019S}$: 55.38 ± 4.24 mm/s, $p < 0.001$; Fig. 1e and f). The cylinder experiment revealed no significant asymmetry of forepaw preference in the 2- or 10-month-old WT or *Lrrk2*$^{-G2019S}$ mice (Fig. 1g). Gait tests were evaluated by footprint analysis. Compared with their respective young counterparts, the aged WT and *Lrrk2*$^{-G2019S}$ mice both reported obvious differences in gait, including shorter stride distance (Fig. 1h and i), wider sway distance (Fig. 1h and k), and longer stance distance (Fig. 1h and j), which intensified with age. However, no changes were found between genotypes. To examine changes in motor learning and coordination, we administered the accelerating rotarod test. The analysis demonstrated significant main effects of age ($F_{(1,51)} = 19.07$, $p < 0.0001$) and gene mutation ($F_{(1,51)} = 48.56$, $p < 0.0001$), with *Lrrk2*$^{-G2019S}$ mice, especially the aged ones, exhibiting a greater propensity to fall, which suggests impaired coordination and decreased stamina. No significant interaction of genotype with age was detected ($F_{(1,51)} = 0.11$, $p = 0.74$) (Fig. 1l). The animals were subsequently evaluated in a trace fear conditioning test for fear memory. The freezing behavior of the two *Lrrk2*$^{-G2019S}$ groups was not markedly decreased when compared with that of the two WT groups, indicating that conditioned fear cues were well retained (Fig. 1m and n). Our findings evidence the characteristic late-onset hyperactivity and a progressive decline in motor coordination that occur in *Lrrk2*$^{-G2019S}$ mice.

### LRRK2 G2019S Mutation Induces Distinct Microglial Morphology Alterations in Mice During Aging

As cerebral LRRK2 is abundantly expressed in microglia and anatomically concentrated in the striatum (STR) and PFC but weakly expressed in the midbrain area (Fig. S1), we performed a quantitative morphological analysis and compared the complexity of microglial process outgrowth in the PFC and DS of *Lrrk2*$^{-G2019S}$ and WT mice at 2 and 10 months of age by staining them for the myeloid cell marker, ionized calcium-binding adapter molecule 1 (Iba1) (Fig. 2). The analysis revealed a more complex microglial morphology in *Lrrk2*$^{-G2019S}$ animals, with more branches and junctions per cell in the PFC at 2 months of age (branches: WT: 117.0 ± 4.15, *Lrrk2*$^{-G2019S}$: 214.2 ± 11.55, $p < 0.0001$; junctions: WT: 49.50 ± 1.70, *Lrrk2*$^{-G2019S}$: 89.31 ± 4.82, $p < 0.0001$; Fig. 2a and c). This change persisted to 10 months of age, although the difference declined. In the DS region, the changes were

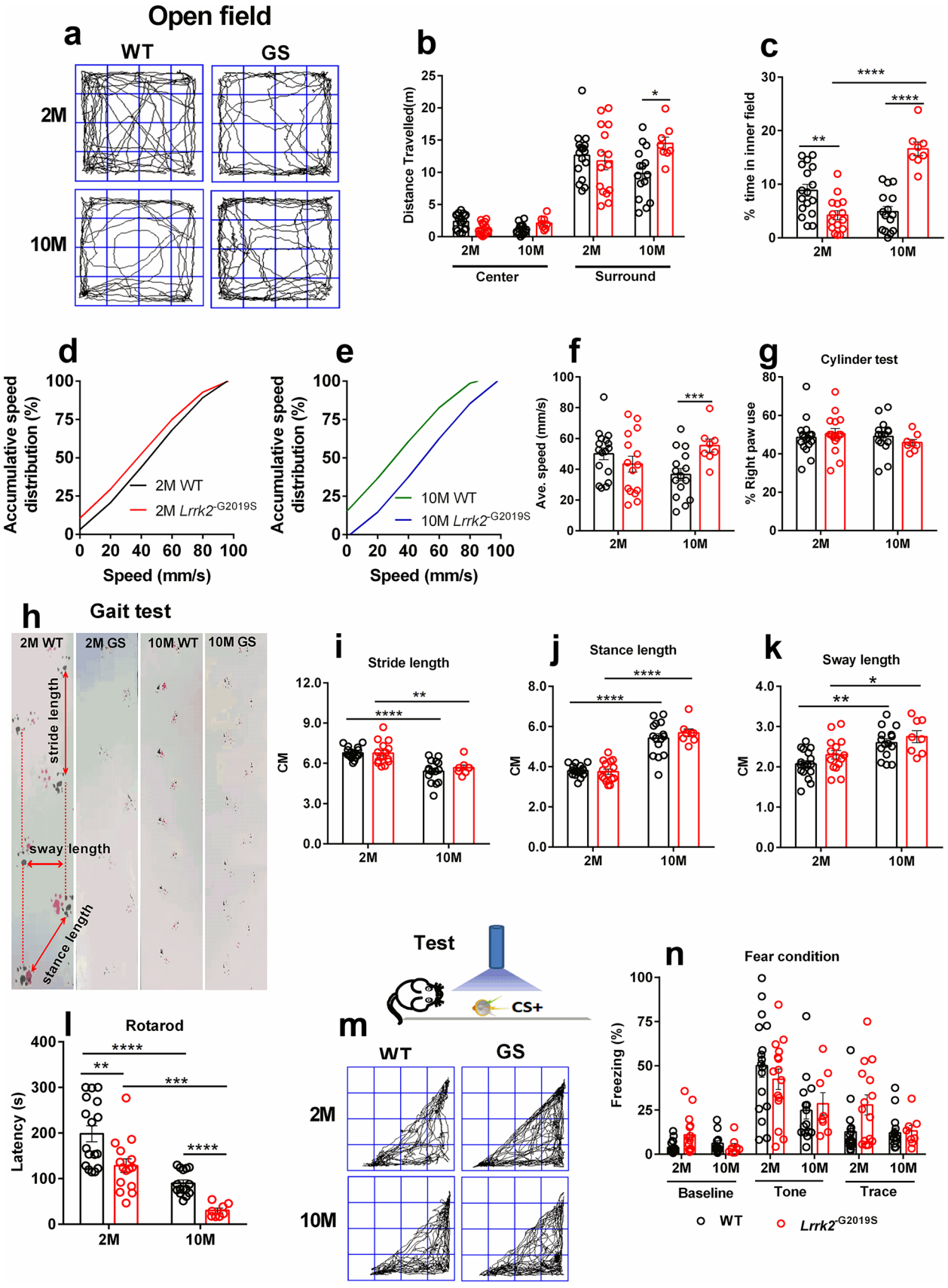
Open field
a
WT
GS
2M
10M
b
Distance Travelled(m)
Center
Surround
c
% time in inner field
d
Accumulative speed distribution (%)
2M WT
2M Lrrk2-G2019S
Speed (mm/s)
e
10M WT
10M Lrrk2-G2019S
f
Ave. speed (mm/s)
g
Cylinder test
% Right paw use
h
Gait test
2M WT
2M GS
10M WT
10M GS
stride length
sway length
stance length
i
Stride length
CM
j
Stance length
k
Sway length
l
Rotarod
Latency (s)
Test
CS+
m
n
Fear condition
Freezing (%)
Baseline
Tone
Trace
WT
Lrrk2-G2019S

◂**Fig. 1** Behavioral performance of LRRK2 G2019S mutant mice and WT mice during aging. **a–f** Exploratory activity and anxiety-like responses in the open field test. **a** Representative track images of mice in the open field. **b** Distance from the central and peripheral area. **c** Percentage of time in the inner field. **d–e** Accumulative (Accum.) frequency of speed distribution in WT and *Lrrk2*$^{-G2019S}$ mice at 2 and 10 months of age. **f** Average speed. **g** Cylinder test. **h** Parameters measured in footprint analysis with dotted lines representing the direction of progression (DoP) of walking. Histograms representing differences in: **i** stride length, **j** stance length, **k** sway length (cm). **l** Rotarod test. **m** Representative track images of mice in the fear conditioning test. **n** Quantification of freezing time on day 2 for 3 min before shock (baseline) and on day 2 for 30 s shock (tone) and after shock (trace) ($n=17$ and 15 for 2-month-old WT and *Lrrk2*$^{-G2019S}$ mice, respectively; $n=15$ and 8 for 10-month-old WT and *Lrrk2*$^{-G2019S}$ mice, respectively). *$p<0.05$, **$p<0.01$, ***$p<0.001$, ****$p<0.0001$

also evident (Fig. 2d and e). The findings suggest that LRRK2 G2019S mutation is involved in the delicate regulation of microglial morphogenesis during aging.

## LRRK2 G2019S Mutation Accelerates Age-Related Loss of DAergic Nerve Fibers in the Dorsal Striatum

We next investigated whether LRRK2 G2019S mutation impacts DAergic nerve fibers during aging. The axonal terminals of DA neurons in the DS were visualized by DAT/TH staining (Fig. 3a). Quantification by confocal microscopy showed that at 2 months of age, the TH$^+$ and DAT density in the DS was significantly reduced in the LRRK2 G2019S group (TH$^+$ density: WT: $112.80\pm5.30$ μm$^2$, *Lrrk2*$^{-G2019S}$: $53.36\pm4.34$ μm$^2$, $p<0.0001$; DAT density: WT: $1056\pm47.43$ μm$^2$, *Lrrk2*$^{-G2019S}$: $424.40\pm23.06$ μm$^2$, $p<0.0001$; Fig. 3b and c). Compared with 10-month-old WT mice, the age-matched group of *Lrrk2*$^{-G2019S}$ mice showed a further decrease in TH$^+$ and DAT density (TH$^+$ density: WT: $113.80\pm4.89$ μm$^2$, *Lrrk2*$^{-G2019S}$: $67.93\pm3.59$ μm$^2$, $p<0.0001$; DAT density: WT: $506.0\pm30.08$ μm$^2$, *Lrrk2*$^{-G2019S}$: $327.60\pm11.84$ μm$^2$, $p<0.01$; Fig. 3b and c). Furthermore, we found that in the LRRK2 G2019S mutant mice, the density and fluorescence intensity of TH + and DAT fibers were loose and weak, as opposed to the tight density and high fluorescence intensity observed in the age-matched wild-type mice (Fig. 3d and e). Altogether, these results suggest that the LRRK2 G2019S mutation induces the loss of DAergic nerve fibers in the striatum during aging.

## LRRK2 G2019S Mutation Triggers Excessive Microglial Refinement of DAergic Fibers During Aging

Given the differences in microglial morphology in the dorsal striatum of the WT and *Lrrk2*$^{-G2019S}$ groups, we next assessed the potential role of microglia in refining DAergic fibers in *Lrrk2*$^{-G2019S}$ mice during aging. The microglial engulfment of DAergic fibers was quantified by acquiring a 3D reconstruction. The results showed that the puncta of TH$^+$ or DAT was phagocytosed by microglia; the orthogonal projection revealed spatial colocalization, which was further confirmed on the 3D surface area (Fig. 4a and d). Quantitative analysis revealed that the average size, number, and total volume of DAT structures were increased in the cells of the 2-month-old *Lrrk2*$^{-G2019S}$ mice (average size: WT: $0.96\pm0.03$ μm$^3$, *Lrrk2*$^{-G2019S}$: $1.49\pm0.10$ μm$^3$, $p<0.0001$; number: WT: $6.53\pm0.42$, *Lrrk2*$^{-G2019S}$: $9.84\pm0.67$, $p<0.001$; total volume: WT: $6.33\pm0.45$ μm$^3$, *Lrrk2*$^{-G2019S}$: $15.41\pm1.54$ μm$^3$, $p<0.0001$; Fig. 4e and g), a difference that persisted in the 10-month-old *Lrrk2*$^{-G2019S}$ group (number: WT: $7.05\pm0.71$, *Lrrk2*$^{-G2019S}$: $9.67\pm1.06$, $p<0.05$; total volume: WT: $9.27\pm0.98$ μm$^3$, *Lrrk2*$^{-G2019S}$: $13.40\pm1.59$ μm$^3$, $p<0.05$; Fig. 4e and g). Compared with the age-matched WT mice, the number and total volume of TH$^+$ structures were increased in the cells of the *Lrrk2*$^{-G2019S}$ mice (number: WT: $3.80\pm0.51$, *Lrrk2*$^{-G2019S}$: $6.05\pm0.55$, $p<0.05$; total volume: WT: $4.11\pm0.63$ μm$^3$, *Lrrk2*$^{-G2019S}$: $7.84\pm0.64$ μm$^3$, $p<0.05$; Fig. 4h and j). Notably, significant increases in the average size and the volume of phagocytic particles were observed in the 10-month-old *Lrrk2*$^{-G2019S}$ mice when compared with the 2-month-old *Lrrk2*$^{-G2019S}$ mice (average size: $p<0.0001$; total volume: $p<0.01$; Fig. 4h and j). These results imply that the increase in microglial phagocytosis induces the markedly decreased DAT and TH$^+$ density in the *Lrrk2*$^{-G2019S}$ mice.

## Middle-aged Lrrk2$^{-G2019S}$ Mice Display an Enhanced Density of Excitatory Synapses in the PFC

Previous studies have reported that *Lrrk2*$^{-G2019S}$ animals were characterized by paradoxical mild hyperactivity (Mancini et al. 2020), which is consistent with our findings (Fig. 1a and c). In order to further analyze the possible causes of hyperactive behavior in the 10-month-old *Lrrk2*$^{-G2019S}$ group, we focused on the prefrontal cortex. Golgi staining revealed a significantly higher dendritic spine density in the PFC of the *Lrrk2*$^{-G2019S}$ mice than in the WT mice (WT: $9.89\pm0.59$ /10 μm, *Lrrk2*$^{-G2019S}$: $13.83\pm0.78$ /10 μm, $p<0.0001$; Fig. 5a and b). However, in the DS region, the opposite results were observed (WT: $16.04\pm0.58$ /10 μm, *Lrrk2*$^{-G2019S}$: $13.39\pm0.60$ /10 μm, $p<0.05$; Fig. 5a and c). We found that the synapses of the 10-month-old *Lrrk2*$^{-G2019S}$ mice were heavily trimmed, which was consistent with the TH$^+$ and DAT refinements (Fig. 3b and c). Postsynaptic density protein 95 (PSD95) is a pivotal postsynaptic scaffolding protein in excitatory neurons (Coley and Gao 2018). In order to investigate whether microglia in the PFC of *Lrrk2*$^{-G2019S}$ mice are defective in synapse elimination, the amount of PSD95 within microglial phagolysosomes in the PFC of 10-month-old *Lrrk2*$^{-G2019S}$ mice or age-matched

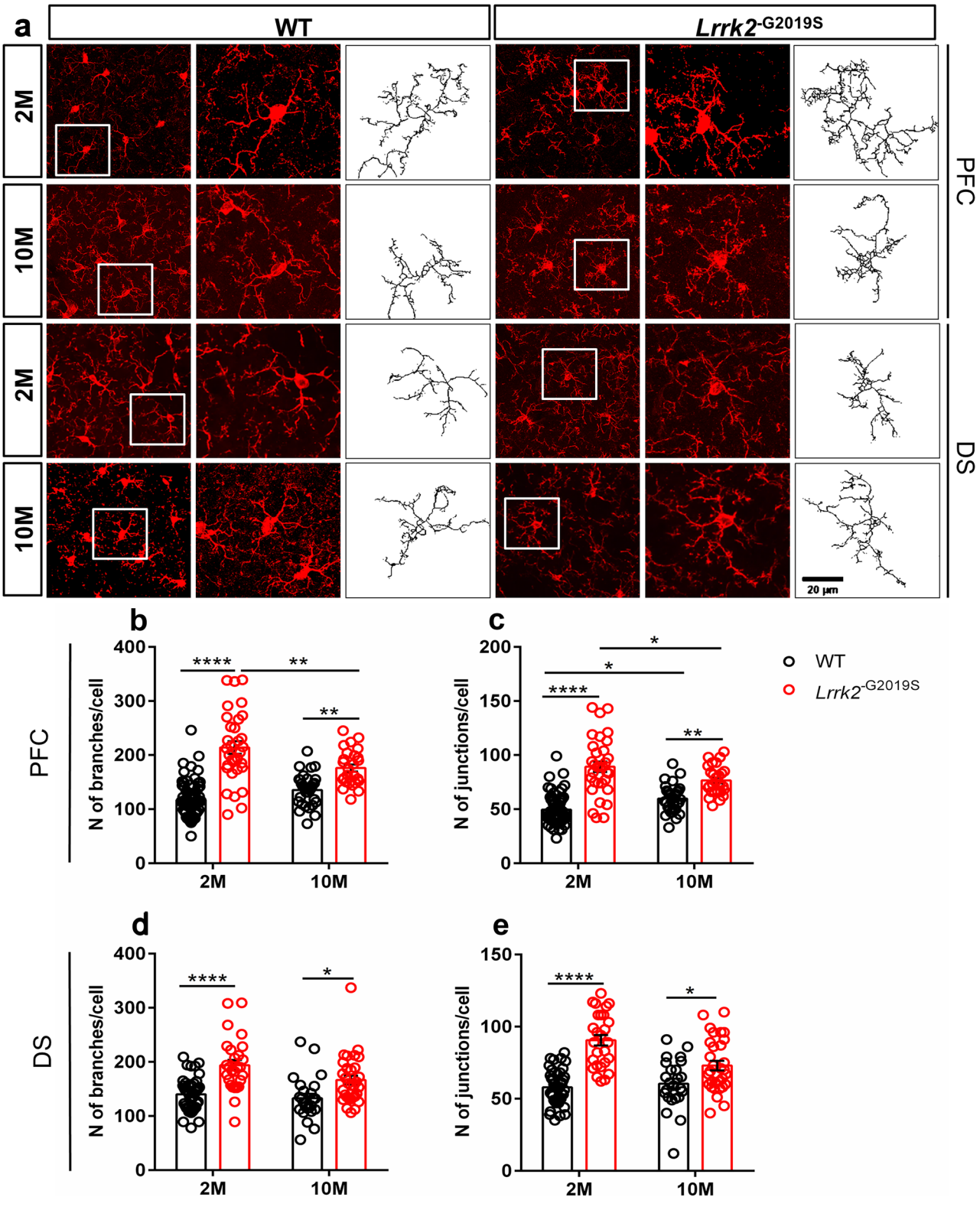
a
WT
Lrrk2-G2019S
2M
10M
2M
10M
PFC
DS
20 μm
b
c
d
e
PFC
DS
N of branches/cell
N of junctions/cell
2M
10M
****
**
*
WT
Lrrk2-G2019S

◂**Fig. 2** Increased microglial complexity in the PFC and DS of 2- and 10-month-old *Lrrk2*$^{-G2019S}$ mice. **a** Confocal fluorescence images showing Iba1/Alexa Fluor-594-labeled microglia (left and middle panels) and skeletonized reconstruction of an individual microglial cell (right panel) in the prefrontal cortex (PFC) and dorsal striatum (DS) of 2- and 10-month-old wild-type (WT) and *Lrrk2*$^{-G2019S}$ mice: white frames marking a single microglial cell, the reconstructed skeletonized image shown in the right panel. Original magnification × 63; Scale bar = 20 µm. Quantitative analysis of total branches (**b** and **d**) and junctions (**c** and **e**) per cell in the PFC and DS. For 2-month-old WT group, $N = 3$ mice, $n = 66$ cells (PFC), $n = 43$ cells (DS); for 10-month-old WT group, $N = 3$ mice, $n = 32$ cells (PFC), $n = 27$ cells (DS); for 2-month-old *Lrrk2*$^{-G2019S}$, $N = 3$ mice, $n = 32$ cells (PFC), $n = 24$ cells (DS); for 10-month-old *Lrrk2*$^{-G2019S}$, $N = 3$ mice, $n = 26$ cells (PFC), $n = 31$ cells (DS). *$p < 0.05$, **$p < 0.01$, ****$p < 0.0001$

WT mice was analyzed by immunofluorescence. A significantly smaller amount of PSD95 puncta was detected in the microglia of the *Lrrk2*$^{-G2019S}$ mice than in those of the WT group (total volume: $p = 0.037$; average size: $p = 0.009$; Fig. 5h and k), paralleled by a higher total amount of PSD95 per field (WT: 9.776 ± 0.29%, *Lrrk2*$^{-G2019S}$: 14.39 ± 0.50%, $p < 0.0001$; Fig. 5d and f). Meanwhile, immunofluorescence analysis revealed an increased density of the excitatory presynaptic marker VGLUT1 (WT: 15.70 ± 0.60%, *Lrrk2*$^{-G2019S}$: 18.00 ± 0.51%, $p < 0.01$; Fig. 5e and g) and an observable decline in VGLUT1 puncta in the microglia of *Lrrk2*$^{-G2019S}$ mice when compared with those of WT mice (total volume: $p = 0.0249$; average size: $p = 0.0019$; Fig. 5l and o). These results show that the synaptic pruning capacity of microglia decreases in the PFC brain region of *Lrrk2*$^{-G2019S}$ mice.

### LRRK2 G2019S Mutation Alters Microglia and Inflammation-Related Molecules in the PFC and Striatum

The above-mentioned findings indicate that the immune response triggered by the LRRK2 G2019S mutation may be an important factor impacting the pathophysiology of PD. To test this possibility, we isolated brain regions and extracted RNA to identify the expressed mRNAs by RT–qPCR analysis. Cluster analysis showed obvious associations among the expression levels of certain genes (Fig. 6a and c), suggesting that LRRK2 G2019S mutation alters the relationships among microglial transcripts with increasing age. Tmem119 and PU.1 were found to be differentially expressed in the PFC region between *Lrrk2*$^{-G2019S}$ and WT mice. Compared with that of the age-matched controls, Tmem119 mRNA ($p < 0.001$) and PU.1 mRNA ($p < 0.001$) were upregulated in the 10-month-old *Lrrk2*$^{-G2019S}$ mice (Fig. 6b). Previous studies have attributed age-related PD physiopathology to neuroinflammation (De Virgilio et al. 2016). Compared with the age-matched controls, TNF-α mRNA ($p < 0.01$), iNOS mRNA ($p < 0.01$), IL-6 mRNA ($p < 0.01$), IFN-γ mRNA ($p < 0.05$), and IL-4 mRNA ($p < 0.05$) were upregulated in the 10-month-old *Lrrk2*$^{-G2019S}$ mice (Fig. 6b and S2). In the STR region, compared with the age-matched controls, IFN-γ mRNA ($p < 0.05$) was upregulated in the 10-month-old *Lrrk2*$^{-G2019S}$ mice (Fig. 6d).

## Discussion

Clinical and experimental studies of PD are dominated by a focus on the degeneration of DAergic neurons and the ensuing abnormalities in the motor system. However, a number of non-motor symptoms, including cognitive and psychiatric symptoms, may appear during the disease course (Huntley and Benson 2020). Previous research reports that *Lrrk2*$^{-G2019S}$ animals are characterized by paradoxical mild hyperactivity (Mancini et al. 2020), which is consistent with our finding. There is evidence that psychiatric behavior is related to synaptic response and synaptic plasticity (Matikainen-Ankney et al. 2018). The present study documents in 10-month-old *Lrrk2*$^{-G2019S}$ mice a remarkable pathogenic finding that the significantly increased spine density and defective microglia mediate excitatory synapse elimination in the PFC. Thus, the increase in excitatory synaptic density in the PFC may contribute to the hyperactivity in *Lrrk2*$^{-G2019S}$ mice. These findings provide a neuroanatomical basis for the observed hyperactivity in middle-aged *Lrrk2*$^{-G2019S}$ mice.

LRRK2 mutation carriers without PD manifestations showed reduced DAT binding at an early stage, which might represent a primary effect on DAT function that is independent of nerve terminal loss and does not become apparent until later in life (Wile et al. 2017). Reduced DAT levels might indicate a decreased density of DAergic neurons, regulatory changes in synaptic terminal density, or a change in transporter expression. In the current study, *Lrrk2*$^{-G2019S}$ mice, especially middle-aged ones, showed an increased propensity to fall during the accelerating rotarod test, implying impaired coordination and decreased stamina. Such primary motor disturbances result principally from the progressive death of DAergic neurons in the substantia nigra and accompanying degenerative loss of DAergic axon terminals within the striatum (Huntley and Benson 2020). Another possibility may lie in the impaired corticostriatal synaptic plasticity, which is considered to be a cellular basis for somatic motor regulation and motor skill learning (Wang et al. 2019). This may be mechanistically explained by our finding that, in the DS region, the synapses of middle-aged *Lrrk2*$^{-G2019S}$ mice are heavily trimmed, accompanied by accelerated refinement of DAergic fibers in the same region of the brain.

Microglia are monocytic immune cells that protect neurons from noxious stimuli, including pathological α-synuclein species, and microglial activation is believed

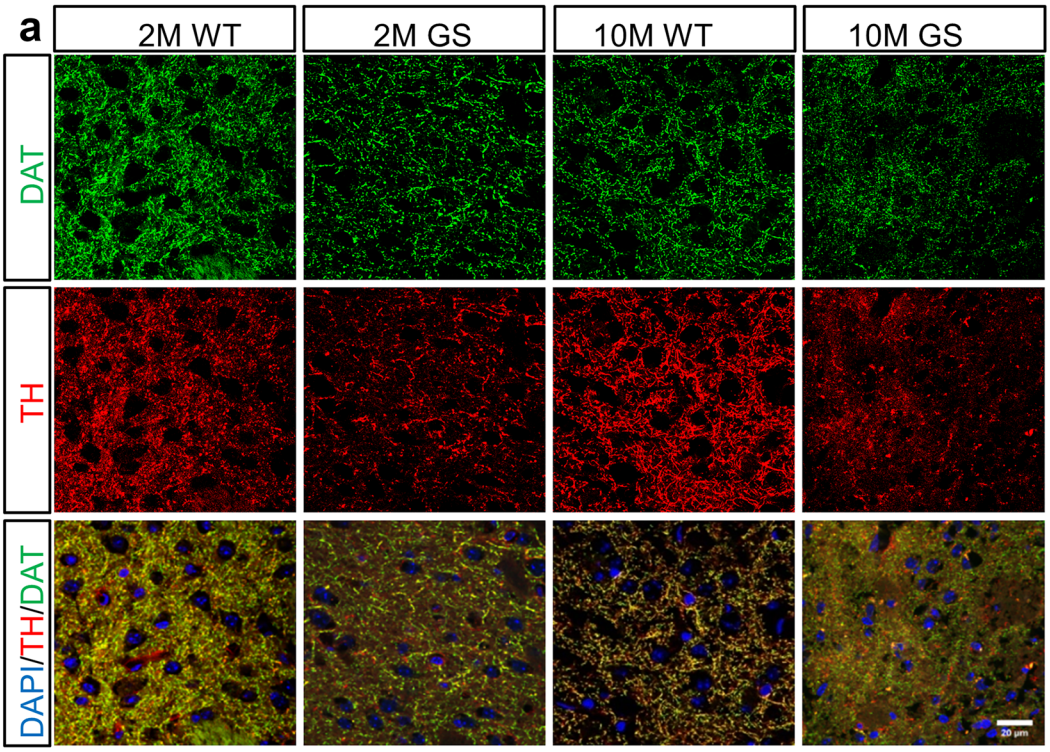
a
2M WT
2M GS
10M WT
10M GS
DAT
TH
DAPI/TH/DAT
20 µm

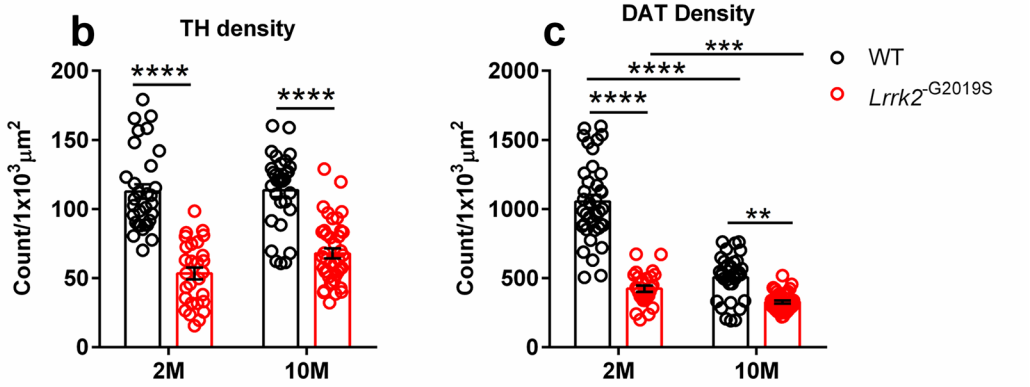
b
TH density
Count/1x10³µm²
****
****
2M
10M
c
DAT Density
***
****
****
**
WT
Lrrk2-G2019S

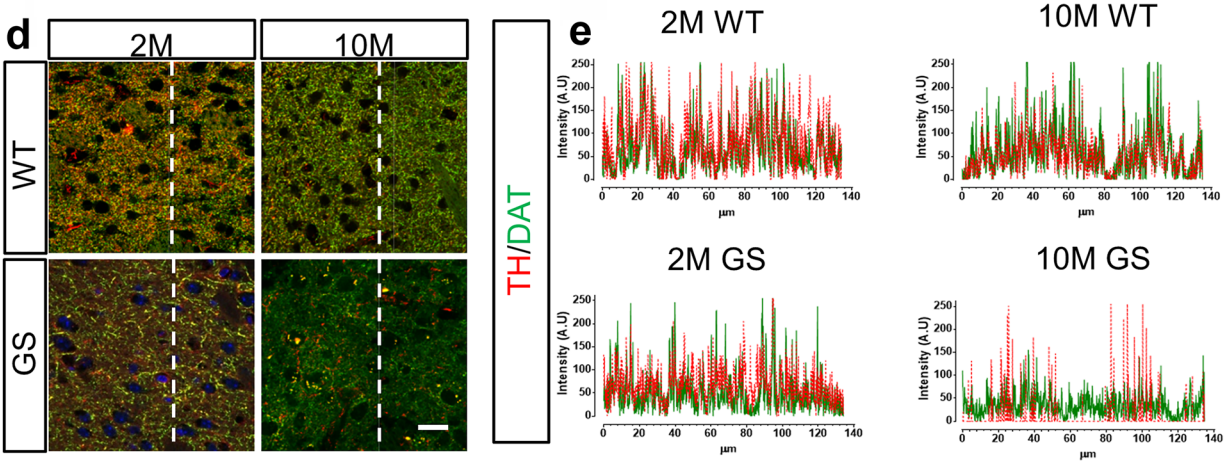
d
2M
10M
WT
GS
TH/DAT
e
2M WT
10M WT
2M GS
10M GS
Intensity (A.U)
µm

◂**Fig. 3** The expression of DAergic nerve fibers in dorsal striatum of *Lrrk2*$^{-G2019S}$ mice. **a** Representative images showing TH (red) and DAT (green) staining in dorsal striatum in the 2- and 10-month-old WT and *Lrrk2*$^{-G2019S}$ mice. DAPI was used to stain the nucleus (blue). Scale bar = 20 µm. **b, c** Density of TH (**b**) and DAT (**c**) in the dorsal striatum of the 2- and 10-month-old WT and *Lrrk2*$^{-G2019S}$(GS) mice ($n = 3$ animals per genotype; $n \geq 4$ sections per animal). **d** Comparison of the density and fluorescence intensity of DAergic nerve fibers within the dorsal striatum among 2- and 10-month-old WT and *Lrrk2*$^{-G2019S}$ mice. The vertical dotted line crossing the axonal terminals projection is 140 µm long from top to bottom. Scale bars = 20 µm. **e** Quantification of the density and fluorescence intensity of $TH^+$ and DAT fibers. ***$p < 0.001$, ****$p < 0.0001$

to contribute to neuroinflammation and neuronal death in PD (Schapansky et al. 2015). LRRK2 is richly expressed in the microglia (Gardet et al. 2010; Hakimi et al. 2011). Recent reports have indicated that LRRK2 G2019S mutation impacts microglial activity, resulting in disordered microglial phagocytosis and migration. Microglia in mice with the LRRK2 G2019S mutation display an increased phagocytic response in vitro (Choi et al. 2015; Dwyer et al. 2020; Kim et al. 2018). Our findings that the complexity of microglial morphology increased in *Lrrk2*$^{-G2019S}$ mice suggest that the LRRK2 G2019S mutation is involved in the delicate regulation of microglial morphogenesis during aging.

Despite the differences in microglial morphology in the striatum of the WT and *Lrrk2*$^{-G2019S}$ groups, the potential role of microglia in refining DAergic fibers in *Lrrk2*$^{-G2019S}$ mice during aging is largely unknown. Our findings reveal that LRRK2 G2019S mutation results in excessive microglial refinement of DAergic fibers during aging. In the current study, the markedly decreased $TH^+$ density in the *Lrrk2*$^{-G2019S}$ mice was attributed to the increased microglial phagocytosis with increasing age. Despite no significant difference in $TH^+$ density between the young and middle-aged groups of *Lrrk2*$^{-G2019S}$, an enlarged volume of phagocytic particles was found, which may be attributed to the abnormally enlarged varicosities of $TH^+$ cells (Liu et al. 2015). With regard to the molecular mechanisms underlying the processes in LRRK2-regulated microglial activation and phagocytosis, one possible explanation may be that LRRK2 orchestrates cytoskeletal components such as actin, tubulin, and ERM proteins. Another alternative may be that the pathological G2019S mutation causes hyperphosphorylation and hyperpolymerization of cytoskeletal components, in turn leading to reactive microglia with enhanced cell activity, migration, and phagocytosis in response to pathological stimuli (Russo et al. 2014).

LRRK2 is involved in neuroinflammation. Specifically, this protein promotes microglial priming via negative regulation of the transcription factors NFAT and NF-κB, leading to intensified immune responses. This suggests that LRRK2 is not directly involved in degenerative processes but rather influences other pathways that lead to neurodegeneration (Schildt et al. 2019). In this study, the results showed that cytokines (IFN-γ, TNF-α, and IL-4) were increased in the PFC region of middle-aged *Lrrk2*$^{-G2019S}$ mice. However, only one cytokine (IFN-γ) was increased in the DS region of middle-aged *Lrrk2*$^{-G2019S}$ mice. The findings suggest that the microenvironment of LRRK2 G2019S mutation causes different expression of cytokines in certain brain regions. In some pathological conditions, microglia produce increased levels of cytotoxic and inflammatory mediators, such as TNF-α, which can reactivate microglia in a positive feedback mechanism (Bras et al. 2020). Similarly, IFN-γ induces reactive phenotypes in microglia associated with morphological changes (Papageorgiou et al. 2016). The secretion of IL-4 by M2-activated macrophages promotes humoral immune responses and downregulates M1-mediated responses. Originally, M2 activation was thought to produce a protective effect. However, evidence shows that M2 cytokines such as IL-4 also result in the induction of some chronic inflammatory processes (Shapouri-Moghaddam et al. 2018; Wynn 2003). Moreover, our results found that the transcription factor PU.1 was increased in the PFC region of middle-aged *Lrrk2*$^{-G2019S}$ mice. PU.1 is critical in the development of myeloid cells and a major regulator of microglial gene expression. PU.1 expression levels are driven by increased pro-inflammatory response (Pimenova et al. 2021; Rustenhoven et al. 2018). These data suggest that microglia in *Lrrk2*$^{-G2019S}$ mice actively participate in the pathogenesis of neuronal damage in neurodegenerative diseases by producing inflammatory mediators. Our findings in the present study provide evidence that microglial activation at DAergic fiber terminals and synapses in the striatum contributes to the severity of motor symptoms and at synapses in the PFC contributes to hyperactive behaviors, supporting the notion that reactive microglia exacerbate the progression of the disease in a region-specific manner. The reason for the differences in microglial reactivity may come from differential cytokine stress between the PFC and DS. Further studies are needed to elucidate fine mechanisms that contribute to the abnormal microglial phagocytosis and refinements of synapses and DAergic fibers during aging.

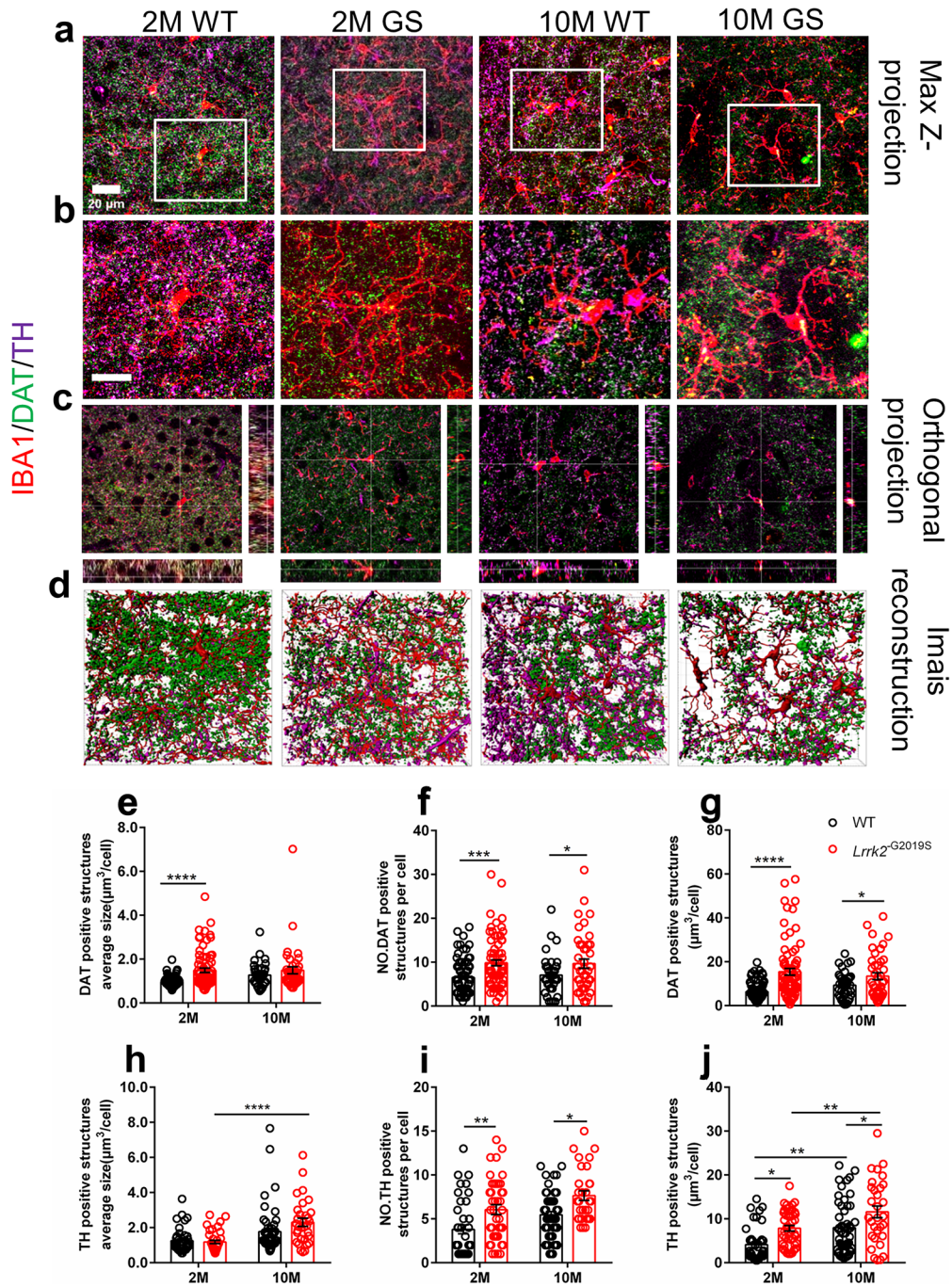


**Fig. 4** Effect of LRRK2 G2019S mutation on the refinement of microglial DAergic fibers during aging. **a** Representative Z projection images of microglia (Iba1$^+$, red) and DAT (green), TH$^+$ (purple) in the dorsal striatum from 2- and 10-month-old WT and *Lrrk2*$^{-G2019S}$ (GS) mice. Scale bar = 20 µm. **b** High resolution of similar regions to the marked area. Scale bar = 30 µm. **c** Representative orthogonal slice images. Scale bar = 20 µm. **d** Representative 3D reconstructions showing DAT/TH$^+$ structures within Iba1$^+$ microglia. Scale bar = 20 µm. **e** Quantification of average size of DAT structure per cell. **f** Number of DAT structures per cell, and **g** total volume of DAT structures per cell (for 2-month-old WT mice, $n = 81$ cells; for 10-month-old WT mice, $n = 38$ cells; for 2-month-old *Lrrk2*$^{-G2019S}$ mice, $n = 74$ cells; for 10-month-old *Lrrk2*$^{-G2019S}$ mice $n = 42$ cells, from three animals per genotype). **h** Quantification of average size of TH$^+$ structure per cell. **i** Number of TH$^+$ structures per cell and **j** total volume of TH$^+$ structures per cell (for 2-month-old WT mice, $n = 40$ cells; for 10-month-old WT mice, $n = 51$ cells; for 2-month-old *Lrrk2*$^{-G2019S}$ mice, $n = 41$ cells; for 10-month-old *Lrrk2*$^{-G2019S}$ mice $n = 31$ cells, from three animals per genotype).*$p < 0.05$, ***$p < 0.001$, ****$p < 0.0001$

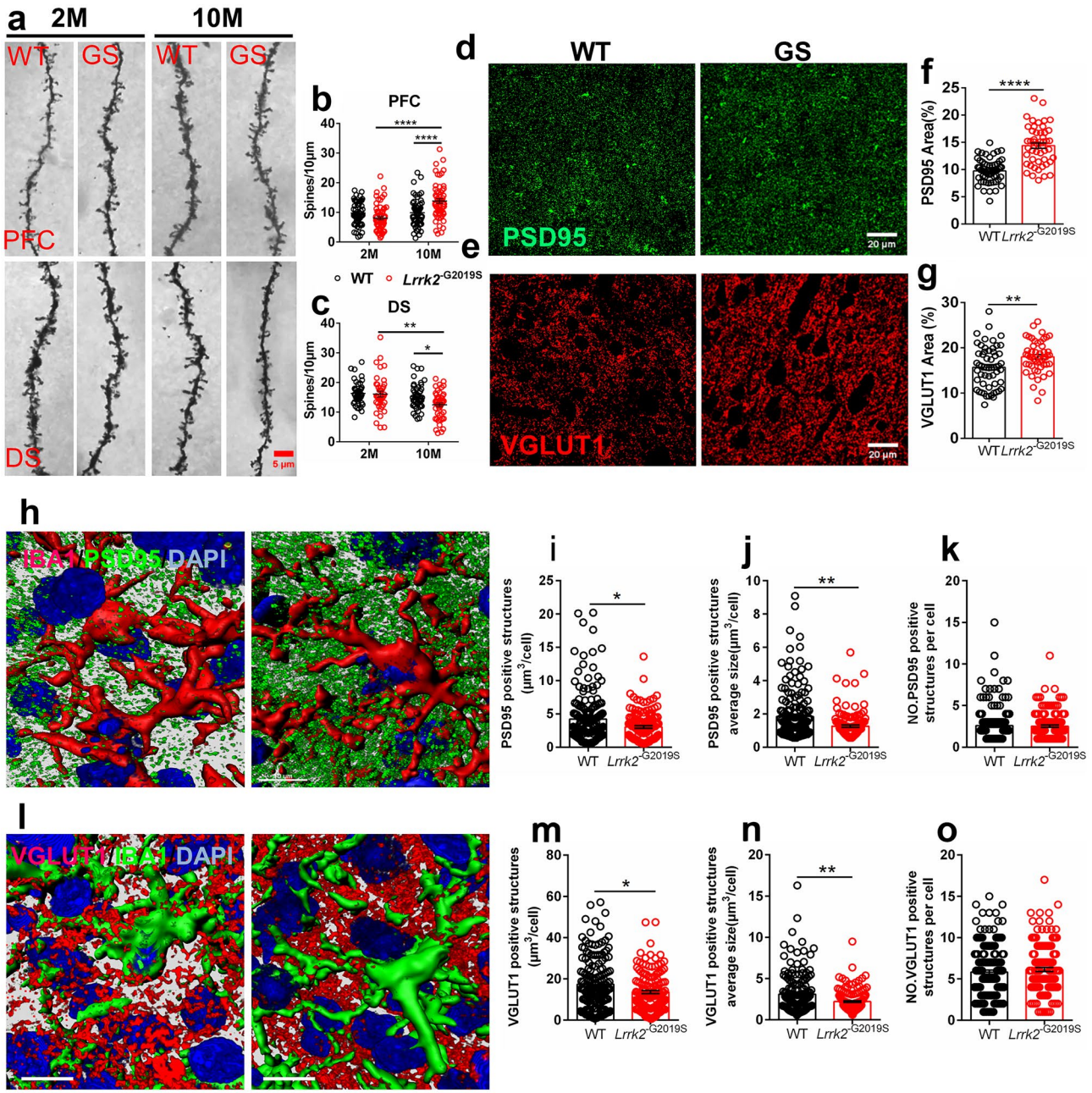


**Fig. 5** The expression of excitatory synapses in the PFC of elderly *Lrrk2*$^{-G2019S}$ mice. **a** Representative images of secondary branches of apical dendrites in the Golgi-Cox-stained PFC and DS of 2- and 10-month-old WT and *Lrrk2*$^{-G2019S}$ (GS) mice. **b, c** Relative quantification of dendritic spines: number of spines/10 μm: $N=3$, $n=60$ dendrites, scale bar = 5 μm. Representative fields (**d** and **e**) and relative quantification (**f** and **g**) of the PFC region of the two 10-month-old groups, stained for PSD95 (for WT group, $N=3$ mice, $n=56$ fields; for *Lrrk2*$^{-G2019S}$ group, $N=3$ mice, $n=50$ fields) and for VGLUT1 (for WT group, $N=3$ mice, $n=57$ fields; for *Lrrk2*$^{-G2019S}$ group, $N=3$ mice, $n=50$ fields). Scale bar = 20 μm. **h** Representative 3D reconstructions showing PSD95-positive structures within Iba1$^{+}$ microglial cells (scale bar = 10 μm). **i** Quantification of PSD95-positive structures (total volume per cell), **j** average size per PSD95-positive structure, and **k** number of PSD95-positive structures per cell (for 10-month-old WT group, $n=163$ cells; for 10-month-old *Lrrk2*$^{-G2019S}$ group, $n=140$ cells, from three animals per genotype. **l** Representative 3D reconstructions showing VGLUT1-positive structures within Iba1$^{+}$ microglia (scale bar = 10 μm). **m** Quantification of the total volume of VGLUT1-positive structures per cell, **n** average size per VGLUT1-positive structure, and **o** number of VGLUT1-positive structures per cell (for 10-month-old WT group, $n=166$ cells; for 10-month-old *Lrrk2*$^{-G2019S}$ group, $n=147$ cells, from three animals per genotype).*$p<0.05$, **$p<0.01$, ****$p<0.0001$

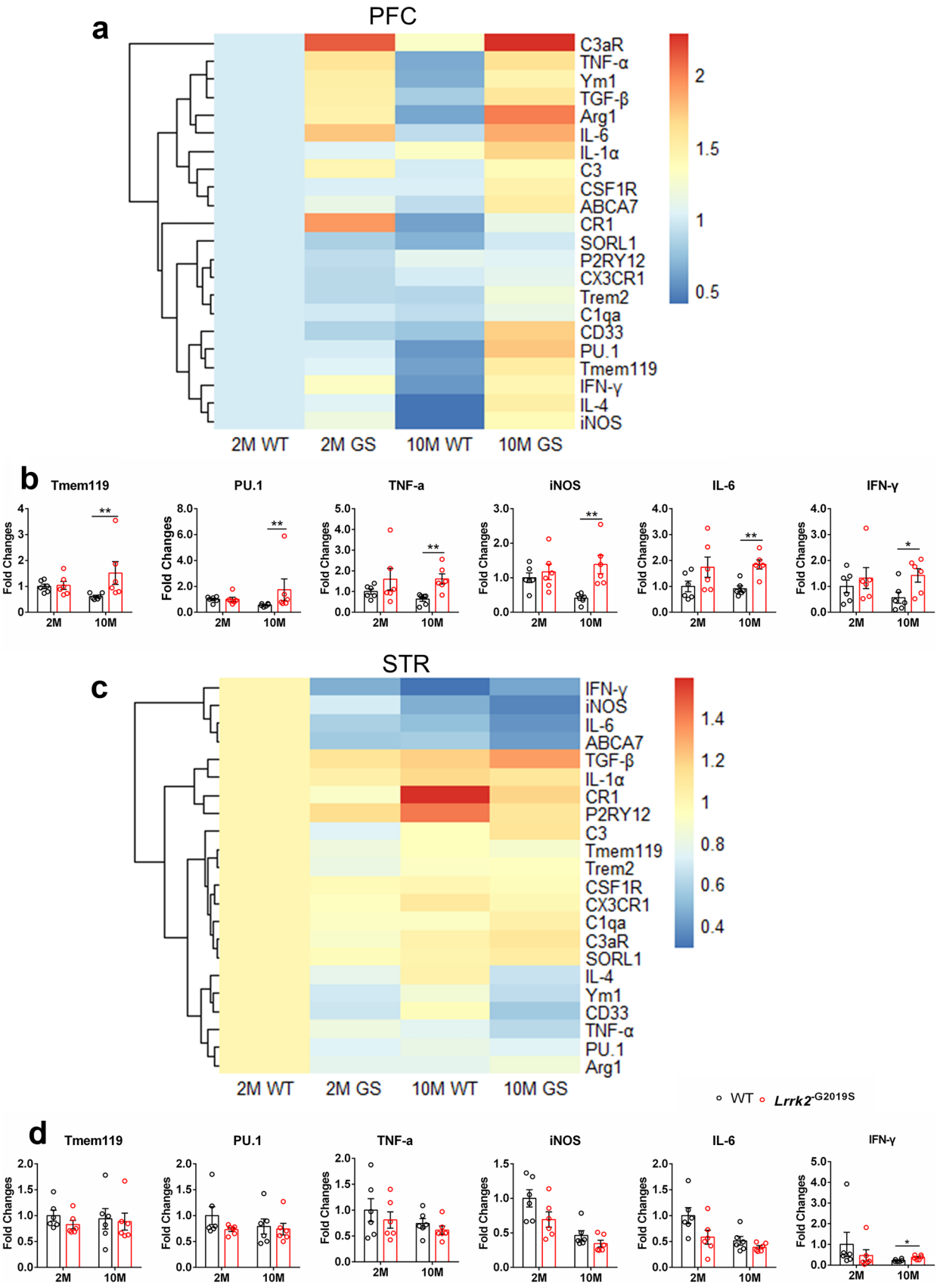
a
PFC
C3aR
TNF-α
Ym1
TGF-β
Arg1
IL-6
IL-1α
C3
CSF1R
ABCA7
CR1
SORL1
P2RY12
CX3CR1
Trem2
C1qa
CD33
PU.1
Tmem119
IFN-γ
IL-4
iNOS
2
1.5
1
0.5
2M WT
2M GS
10M WT
10M GS
b
Tmem119
PU.1
TNF-a
iNOS
IL-6
IFN-γ
Fold Changes
2M
10M
c
STR
IFN-γ
iNOS
IL-6
ABCA7
TGF-β
IL-1α
CR1
P2RY12
C3
Tmem119
Trem2
CSF1R
CX3CR1
C1qa
C3aR
SORL1
IL-4
Ym1
CD33
TNF-α
PU.1
Arg1
1.4
1.2
1
0.8
0.6
0.4
2M WT
2M GS
10M WT
10M GS
WT
Lrrk2-G2019S
d
Tmem119
PU.1
TNF-a
iNOS
IL-6
IFN-γ
Fold Changes
2M
10M

◂**Fig. 6** The expression of inflammation and microglia-related molecules in PFC and striatum of *Lrrk2*$^{-G2019S}$ mice. **a, c** Cluster analysis of mRNA expression of phagocytic receptors and inflammation-related molecules from the PFC (**a**) / striatum (STR) (**c**) of the 2- and 10-month-old WT and *Lrrk2*$^{-G2019S}$ mice. **b, d** Relative mRNA expression of Tmem119, PU.1, TNF-α, iNOS, IL-6, and IFN-γ from the PFC (**b**) /STR (**d**). Levels of the mRNAs were normalized to the levels of GAPDH mRNA in the same sample and values are expressed as fold change ($n=6$ mice per group). $^{*}p<0.05$, $^{**}p<0.01$

## Conclusion

In summary, the study provides a novel and detailed microglial aberrant morphogenesis of LRRK2 mutation in vivo and deepens our comprehension of the relationship among behavior, neuron-microglial interaction, and molecular phenotypes in the PD model of LRRK2 G2019S during aging. These findings indicate that LRRK2 G2019S mutation impacts microglial morphogenesis and activity and remodels the transcription landscape of microglial inflammatory molecules, thereby leading to abnormal microglial phagocytosis, synaptic pruning, and loss of DAergic fibers during aging, and, eventually, PD-related behavioral abnormalities.

**Supplementary Information** The online version contains supplementary material available at https://doi.org/10.1007/s12031-021-01896-6.

**Acknowledgements** We would like to thank Professor Hongzhi Huang from School of Arts and Sciences of Fujian Medical University for his kind proofreading and polishing of this manuscript.

**Author Contributions** Xiaodong Pan conceived the study design and Qiuyang Zhang conducted the animal study and quantitative analysis, and they were chief contributors in writing the manuscript. Xiaojuan Cheng, Wei Wu, Siyu Yang and Hanlin You performed the animal behavior study and histochemical experiments. Xiaochun Chen, Nan Liu and Zucheng Ye reviewed the manuscript. All authors read and approved the final manuscript.

**Funding** This work was supported by grants from the National Natural Science Foundation of China (No. 81771179, No. 82071175); Natural Science Foundation (Key Project) of Fujian Province, China (No. 2020J02022); Fujian Provincial Health-Education Joint Research Project (No. WKJ2016-2–08); Startup Fund for scientific research from Fujian Medical University (No. 2017XQ2023, No. 2017XQ2035).

**Availability of Data and Materials** The datasets used and/or analyzed in this study are available from the corresponding authors on reasonable request.

## Declarations

**Ethics Approval and Consent to Participate** All animal experimental procedures conformed to the National Institute of Health Guidelines for the Care and Use of Laboratory Animals and were approved by the Institutional Animal Care and Use Committee of Fujian Medical University.

**Consent for Publication** All authors read and approved the final manuscript.

**Disclosures** The authors declare that they have no competing interests.

## References

Arganda-Carreras I, Fernandez-Gonzalez R, Munoz-Barrutia A, Ortiz-De-Solorzano C (2010) 3D reconstruction of histological sections: Application to mammary gland tissue. Microsc Res Tech 73(11):1019–1029. https://doi.org/10.1002/jemt.20829

Bonnard C, Navaratnam N, Ghosh K, Chan PW, Tan TT, Pomp O, Ng AYJ, Tohari S, Changede R, Carling D, Venkatesh B, Altunoglu U, Kayserili H, Reversade B (2020) A loss-of-function NUAK2 mutation in humans causes anencephaly due to impaired Hippo-YAP signaling. J Exp Med 217 (12). https://doi.org/10.1084/jem.20191561

Bras JP, Bravo J, Freitas J, Barbosa MA, Santos SG, Summavielle T, Almeida MI (2020) TNF-alpha-induced microglia activation requires miR-342: impact on NF-kB signaling and neurotoxicity. Cell Death Dis 11(6):415. https://doi.org/10.1038/s41419-020-2626-6

Choi C, Kim A, Byun JW, Baik JS, Yun H, Kim A, Jung CR, Song Q, Shin ES, Seo H, Suh YH, Jou I, Park BJ, Kang HC, Joe EH (2015) LRRK2 G2019S mutation attenuates microglial motility by inhibiting focal adhesion kinase. Nat Commun 6:8255. https://doi.org/10.1038/ncomms9255

Chou JS, Chen CY, Chen YL, Weng YH, Yeh TH, Lu CS, Chang YM, Wang HL (2014) (G2019S) LRRK2 causes early-phase dysfunction of SNpc dopaminergic neurons and impairment of corticostriatal long-term depression in the PD transgenic mouse. Neurobiol Dis 68:190–199. https://doi.org/10.1016/j.nbd.2014.04.021

Coley AA, Gao WJ (2018) PSD95: A synaptic protein implicated in schizophrenia or autism? Prog Neuropsychopharmacol Biol Psychiatry 82:187–194. https://doi.org/10.1016/j.pnpbp.2017.11.016

De Virgilio A, Greco A, Fabbrini G, Inghilleri M, Rizzo MI, Gallo A, Conte M, Rosato C, Ciniglio Appiani M, de Vincentiis M (2016) Parkinson's disease: Autoimmunity and neuroinflammation. Autoimmun Rev 15(10):1005–1011. https://doi.org/10.1016/j.autrev.2016.07.022

Dwyer Z, Rudyk C, Thompson A, Farmer K, Fenner B, Fortin T, Derksen A, Sun H, Hayley S, Clint (2020) Leucine-rich repeat kinase-2 (LRRK2) modulates microglial phenotype and dopaminergic neurodegeneration. Neurobiol Aging 91:45–55. https://doi.org/10.1016/j.neurobiolaging.2020.02.017

Fernagut PO, Diguet E, Labattu B, Tison F (2002) A simple method to measure stride length as an index of nigrostriatal dysfunction in mice. J Neurosci Methods 113(2):123–130. https://doi.org/10.1016/s0165-0270(01)00485-x

Filipello F, Morini R, Corradini I, Zerbi V, Canzi A, Michalski B, Erreni M, Markicevic M, Starvaggi-Cucuzza C, Otero K, Piccio L, Cignarella F, Perrucci F, Tamborini M, Genua M, Rajendran L, Menna E, Vetrano S, Fahnestock M, Paolicelli RC, Matteoli M (2018) The microglial innate immune receptor TREM2 is required for synapse elimination and normal brain connectivity. Immunity 48 (5):979–991.e978. https://doi.org/10.1016/j.immuni.2018.04.016

Gardet A, Benita Y, Li C, Sands BE, Ballester I, Stevens C, Korzenik JR, Rioux JD, Daly MJ, Xavier RJ, Podolsky DK (2010) LRRK2 is involved in the IFN-gamma response and host response to pathogens. J Immunol 185(9):5577–5585. https://doi.org/10.4049/jimmunol.1000548

Giesert F, Hofmann A, Burger A, Zerle J, Kloos K, Hafen U, Ernst L, Zhang J, Vogt-Weisenhorn DM, Wurst W (2013) Expression analysis of Lrrk1, Lrrk2 and Lrrk2 splice variants in mice. PLoS One 8(5):e63778. https://doi.org/10.1371/journal.pone.0063778

Hakimi M, Selvanantham T, Swinton E, Padmore RF, Tong Y, Kabbach G, Venderova K, Girardin SE, Bulman DE, Scherzer CR, LaVoie MJ, Gris D, Park DS, Angel JB, Shen J, Philpott DJ, Schlossmacher MG (2011) Parkinson's disease-linked LRRK2 is expressed in circulating and tissue immune cells and upregulated following recognition of microbial structures. J Neural Transm 118(5):795–808. https://doi.org/10.1007/s00702-011-0653-2

Harry GJ (2013) Microglia during development and aging. Pharmacol Ther 139(3):313–326. https://doi.org/10.1016/j.pharmthera.2013.04.013

Healy DG, Falchi M, O'Sullivan SS, Bonifati V, Durr A, Bressman S, Brice A, Aasly J, Zabetian CP, Goldwurm S, Ferreira JJ, Tolosa E, Kay DM, Klein C, Williams DR, Marras C, Lang AE, Wszolek ZK, Berciano J, Schapira AHV, Lynch T, Bhatia KP, Gasser T, Lees AJ, Wood NW (2008) Phenotype, genotype, and worldwide genetic penetrance of LRRK2-associated Parkinson's disease: a case-control study. Lancet Neurol 7(7):583–590. https://doi.org/10.1016/s1474-4422(08)70117-0

Ho M (2019) Microglia in Parkinson's disease. Adv Exp Med Biol 1175:335–353. https://doi.org/10.1007/978-981-13-9913-8_13

Huntley GW, Benson DL (2020) Origins of parkinson's disease in brain development: insights from early and persistent effects of LRRK2-G2019S on striatal circuits. Front Neurosci 14:265. https://doi.org/10.3389/fnins.2020.00265

Ikegami A, Haruwaka K, Wake H (2019) Microglia: Lifelong modulator of neural circuits. Neuropathology : Official Journal of the Japanese Society of Neuropathology 39(3):173–180. https://doi.org/10.1111/neup.12560

Ip CW, Klaus LC, Karikari AA, Visanji NP, Brotchie JM, Lang AE, Volkmann J, Koprich JB (2017) AAV1/2-induced overexpression of A53T-alpha-synuclein in the substantia nigra results in degeneration of the nigrostriatal system with Lewy-like pathology and motor impairment: a new mouse model for Parkinson's disease. Acta Neuropathol Commun 5(1):11. https://doi.org/10.1186/s40478-017-0416-x

Kim KS, Marcogliese PC, Yang J, Callaghan SM, Resende V, Abdel-Messih E, Marras C, Visanji NP, Huang J, Schlossmacher MG, L Trinkle-Mulcahy L, Slack RS, Lang AE, Canadian Lrrk2 in Inflammation T, Park DS (2018) Regulation of myeloid cell phagocytosis by LRRK2 via WAVE2 complex stabilization is altered in Parkinson's disease. Proc Natl Acad Sci USA 115 22 E5164 E5173. https://doi.org/10.1073/pnas.1718946115

Kundey SMA, Bajracharya A, Boettger-Tong H, Fountain SB, Rowan JD (2019) Sex differences in serial pattern learning in mice. Behavioural processes 168:103958. https://doi.org/10.1016/j.beproc.2019.103958

Lee J, Lee S, Ryu YJ, Lee D, Kim S, Seo JY, Oh E, Paek SH, Kim SU, Ha CM, Choi SY, Kim KT (2019) Vaccinia-related kinase 2 plays a critical role in microglia-mediated synapse elimination during neurodevelopment. Glia 67(9):1667–1679. https://doi.org/10.1002/glia.23638

Liu G, Sgobio C, Gu X, Sun L, Lin X, Yu J, Parisiadou L, Xie C, Sastry N, Ding J, Lohr KM, Miller GW, Mateo Y, Lovinger DM, Cai H (2015) Selective expression of Parkinson's disease-related Leucine-rich repeat kinase 2 G2019S missense mutation in midbrain dopaminergic neurons impairs dopamine release and dopaminergic gene expression. Hum Mol Genet 24(18):5299–5312. https://doi.org/10.1093/hmg/ddv249

Mancini A, Mazzocchetti P, Sciaccaluga M, Megaro A, Bellingacci L, Beccano-Kelly DA, Di Filippo M, Tozzi A, Calabresi P (2020) From synaptic dysfunction to neuroprotective strategies in genetic parkinson's disease: Lessons From LRRK2. Front Cell Neurosci 14:158. https://doi.org/10.3389/fncel.2020.00158

Mandemakers W, Snellinx A, O'Neill MJ, de Strooper B (2012) LRRK2 expression is enriched in the striosomal compartment of mouse striatum. Neurobiol Dis 48(3):582–593. https://doi.org/10.1016/j.nbd.2012.07.017

Matikainen-Ankney BA, Kezunovic N, Menard C, Flanigan ME, Zhong Y, Russo SJ, Benson DL, Huntley GW (2018) Parkinson's disease-linked LRRK2-G2019S mutation alters synaptic lasticity and promotes resilience to chronic social stress in young adulthood. J Neurosci 38(45):9700–9711. https://doi.org/10.1523/JNEUROSCI.1457-18.2018

Nolan SO, Reynolds CD, Smith GD, Holley AJ, Escobar B, Chandler MA, Volquardsen M, Jefferson T, Pandian A, Smith T, Huebschman J, Lugo JN (2017) Deletion of Fmr1 results in sex-specific changes in behavior. Brain and Behav 7(10):e00800. https://doi.org/10.1002/brb3.800

Novello S, Arcuri L, Dovero S, Dutheil N, Shimshek DR, Bezard E, Morari M (2018) G2019S LRRK2 mutation facilitates alpha-synuclein neuropathology in aged mice. Neurobiol Dis 120:21–33. https://doi.org/10.1016/j.nbd.2018.08.018

Pan RY, Ma J, Kong XX, Wang XF, Li SS, Qi XL, Yan YH, Cheng J, Liu Q, Jin W, Tan CH, Yuan Z (2019) Sodium rutin ameliorates Alzheimer's disease-like pathology by enhancing microglial amyloid-beta clearance. Sci Adv 5 (2):eaau6328. https://doi.org/10.1126/sciadv.aau6328

Papageorgiou IE, Lewen A, Galow LV, Cesetti T, Scheffel J, Regen T, Hanisch UK, Kann O (2016) TLR4-activated microglia require IFN-gamma to induce severe neuronal dysfunction and death in situ. Proc Natl Acad Sci U S A 113(1):212–217. https://doi.org/10.1073/pnas.1513853113

Pimenova AA, Herbinet M, Gupta I, Machlovi SI, Bowles KR, Marcora E, Goate AM (2021) Alzheimer's-associated PU.1 expression levels regulate microglial inflammatory response. Neurobiol dis 148:105217. https://doi.org/10.1016/j.nbd.2020.105217

Russo I, Bubacco L, Greggio E (2014) LRRK2 and neuroinflammation: partners in crime in Parkinson's disease? J Neuroinflammation 11(52):52. https://doi.org/10.1186/1742-2094-11-52

Rustenhoven J, Smith AM, Smyth LC, Jansson D, Scotter EL, Swanson MEV, Aalderink M, Coppieters N, Narayan P, Handley R, Overall C, Park TIH, Schweder P, Heppner P, Curtis MA, Faull RLM, Dragunow M (2018) PU.1 regulates Alzheimer's disease-associated genes in primary human microglia. Mol Neurodegener 13 (1):44. https://doi.org/10.1186/s13024-018-0277-1

Schapansky J, Nardozzi JD, LaVoie MJ (2015) The complex relationships between microglia, alpha-synuclein, and LRRK2 in Parkinson's disease. Neuroscience 302:74–88. https://doi.org/10.1016/j.neuroscience.2014.09.049

Schildt A, Walker MD, Dinelle K, Miao Q, Schulzer M, O'Kusky J, Farrer MJ, Doudet DJ, Sossi V (2019) Single inflammatory trigger leads to neuroinflammation in LRRK2 rodent model without degeneration of dopaminergic neurons. J Parkinsons Dis 9(1):121–139. https://doi.org/10.3233/JPD-181446

Sellgren C, Gracias J, Watmuff B, Biag J, Thanos J, Whittredge P, Fu T, Worringer K, Brown H, Wang J, Kaykas A, Karmacharya R, Goold C, Sheridan S, Perlis R (2019) Increased synapse elimination by microglia in schizophrenia patient-derived models of synaptic pruning. Nat Neurosci 22(3):374–385. https://doi.org/10.1038/s41593-018-0334-7

Shapouri-Moghaddam A, Mohammadian S, Vazini H, Taghadosi M, Esmaeili SA, Mardani F, Seifi B, Mohammadi A, Afshari JT, Sahebkar A (2018) Macrophage plasticity, polarization, and function in health and disease. J Cell Physiol 233(9):6425–6440. https://doi.org/10.1002/jcp.26429

Sheerin UM, Houlden H, Wood NW (2014) Advances in the Genetics of Parkinson's Disease: A Guide for the Clinician. Mov Disord Clin Pract 1(1):3–13. https://doi.org/10.1002/mdc3.12000

Wang Z, Hou L, Wang D (2019) Effects of exercise-induced fatigue on the morphology of asymmetric synapse and synaptic protein

levels in rat striatum. Neurochem Int 129:104476. https://doi.org/10.1016/j.neuint.2019.104476

Wile DJ, Agarwal PA, Schulzer M, Mak E, Dinelle K, Shahinfard E, Vafai N, Hasegawa K, Zhang J, McKenzie J, Neilson N, Strongosky A, Uitti RJ, Guttman M, Zabetian CP, Ding Y-S, Adam M, Aasly J, Wszolek ZK, Farrer M, Sossi V, Stoessl AJ (2017) Serotonin and dopamine transporter PET changes in the premotor phase of LRRK2 parkinsonism: cross-sectional studies. Lancet Neurol 16(5):351–359. https://doi.org/10.1016/s1474-4422(17)30056-x

Wynn TA (2003) IL-13 effector functions. Annu Rev Immunol 21:425–456. https://doi.org/10.1146/annurev.immunol.21.120601.141142

Xiao Q, Yang S, Le W (2015) G2019S LRRK2 and aging confer susceptibility to proteasome inhibitor-induced neurotoxicity in nigrostriatal dopaminergic system. J Neural Transm 122(12):1645–1657. https://doi.org/10.1007/s00702-015-1438-9

Xu Q, Shenoy S, Li C (2012) Mouse models for LRRK2 Parkinson's disease. Parkinsonism Relat Disord 18:S186–S189. https://doi.org/10.1016/s1353-8020(11)70058-x

Zhang Y, Wu Q, Zhang L, Wang Q, Yang Z, Liu J, Feng L (2019) Caffeic acid reduces A53T alpha-synuclein by activating JNK/Bcl-2-mediated autophagy in vitro and improves behaviour and protects dopaminergic neurons in a mouse model of Parkinson's disease. Pharmacol Res 150:104538. https://doi.org/10.1016/j.phrs.2019.104538